IFA 1999

TRANSONIC FLUTTER SUPPRESSION CONTROL LAW
DESIGN, ANALYSIS AND WIND TUNNEL RESULTS

Vivek Mukhopadhyay
NASA Langley Research Center, Hampton, VA,USA

5 32 - 08

381334

Abstract

The benchmark active controls technology and wind tunnel test program at NASA Langley Research Center was started with the objective to investigate the nonlinear, unsteady aerodynamics and active flutter suppression of wings in transonic flow. The paper will present the flutter suppression control law design process, numerical nonlinear simulation and wind tunnel test results for the NACA 0012 benchmark active control wing model. The flutter suppression control law design processes using (1) classical, (2) linear quadratic Gaussian (LQG), and (3) minimax techniques are described. A unified general formulation and solution for the LQG and minimax approaches, based on the steady state differential game theory is presented. Design considerations for improving the control law robustness and digital implementation are outlined. It was shown that simple control laws when properly designed based on physical principles, can suppress flutter with limited control power even in the presence of transonic shocks and flow separation. In wind tunnel tests in air and heavy gas medium, the closed-loop flutter dynamic pressure was increased to the tunnel upper limit of 200 psf. The control law robustness and performance predictions were verified in highly nonlinear flow conditions, gain and phase perturbations, and spoiler deployment. A non-design plunge instability condition was also successfully suppressed.

Introduction

The benchmark active controls technology (BACT) and wind tunnel test program at NASA Langley Research Center was started with the objective to investigate the nonlinear, unsteady aerodynamics and active flutter suppression of wings in transonic flow. Under the initial wind tunnel test program, a NACA 0012 airfoil rectangular wing, equipped with pressure transducers, active trailing edge control surface, and two spoilers were constructed for active flutter suppression tests. The model was mounted on a pitch and plunge apparatus in the NASA Transonic Dynamics Tunnel in order to test flutter suppression control laws and measure unsteady pressure distributions in nonlinear flows with oscillating shocks and boundary layer separation. It was necessary to develop a flutter suppression system that would be stable under these flow uncertainties.

This paper describes flutter suppression control law design processes using classical and unified linear-quadratic Gaussian minimax techniques. A unified general formulation for the linear quadratic Gaussian and minimax methods based on the steady state differential game theory is presented. Lessons learned in evaluating and improving the singular value based multi-input multi-output system robustness are described. Design considerations for digital implementation are outlined. Numerical simulation of the control law performance, and wind-tunnel test results for flutter suppression, are also presented.
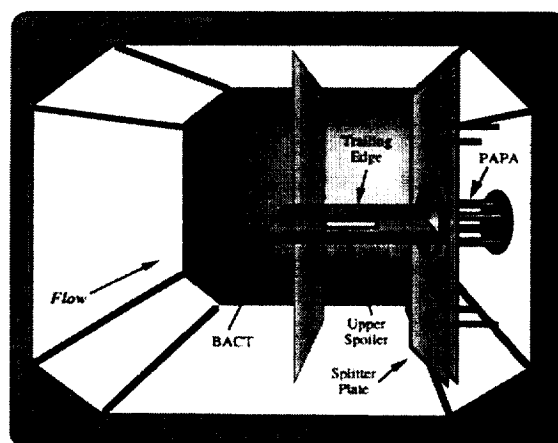

Fig. 1 BACT model test setup in wind tunnel

Wind Tunnel Model Description

A perspective view of the BACT model test set up on the Pitch and Plunge Apparatus (PAPA) in the wind tunnel is shown in Fig. 1. Fig. 2 shows the control surface and sensor locations. The rigid wing section has pitch and plunge degrees of freedom. The accelerometer sensors are located near the section leading edge (zle) and trailing edge (zte) at the section inboard. An identical pair of sensors is located at the section outboard as a spare. The partial span spoilers are located on the upper and lower surfaces, just ahead of the trailing edge control surface. Each of the control surfaces stretched over 30% of the span and 25% of the chord. The bending and torsion frequencies of the PAPA mounted NACA 0012 wing model were 3.3 Hz and 5.2 Hz respectively.
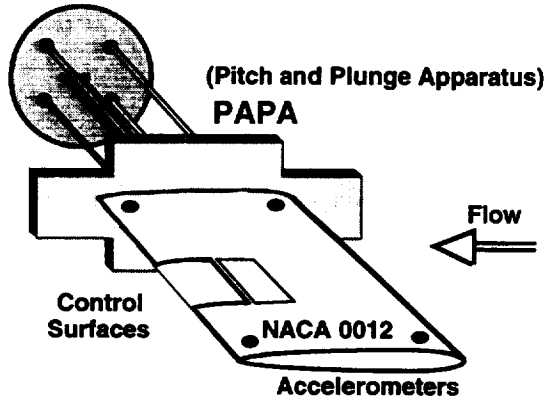
Fig. 2 NACA 0012 BACT wing on PAPA.

Preliminary Analysis

The preliminary analysis, control surface sizing, and flutter suppression control law design were based on the analytical state-space equations of motion of the BACT wing model.[1-4] These equations were developed analytically, using structural dynamic analysis and unsteady doublet lattice aerodynamics with rational polynomial approximations[5]. These linear state space equations consisted of 14 States (plunge, pitch, plunge rate, pitch rate, 3 aerodynamic states for plunge, 3 aerodynamic states for pitch, 2 trailing edge flap actuator states, 2 Dryden gust states), 2 inputs (actuator command and gust input noise) and 7 outputs (zte and zle acceleration, flap command, flap deflection, rate, acceleration, and gust velocity). This 14th order state space equation was used for classical control law design and for performance simulation and verification purposes. For the optimal control law design purposes and for presentation of the design data in a concise form, the 14th order state-space equations were reduced to 4th state-space equations, using residualization and Schur's balanced reduction method[6,7]. First, it was reduced to an 8th order system using residualization technique, in which only the static part of all modes above 15 Hz were retained. The resulting 8th order system was then balanced and the four states of the system with largest balanced singular values were retained. A sample of the 4th order model design data is presented in the Appendix.

Open-loop Responses

The analytical open-loop flutter dynamic pressure in air was 128 pounds per square feet (psf) at a flutter frequency of 4.5 Hz. Fig. 3 shows the response of the wing trailing edge and leading edge accelerometers due to a 1 degree step input of the trailing edge control surface in air at 225 psf dynamic pressure. The primary plunge motion mixed with small pitch diverges rapidly. The unsteady lift forces oscillate about 8 lbs mean lift and

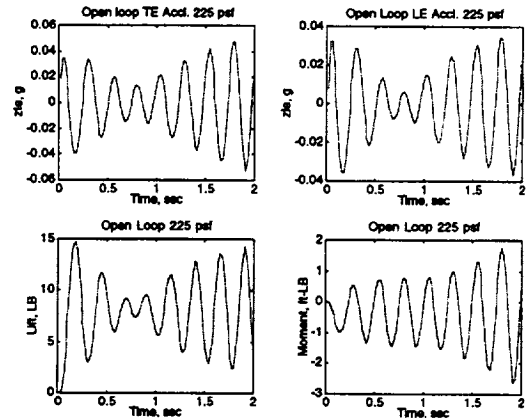diverges at the rate of 6 lbs/sec. The moment diverges at a rate of 1 lb/sec.

Fig. 3 Open loop transient responses in air at 225 psf.

Frequency Responses

The open loop frequency responses were studied using this 14th order plant model, to select a possible candidate for feedback signal in the flutter suppression control law design. The Bode diagram of the trailing edge and leading edge accelerometers (zte) and (zle) and their difference $(zte-zle)$ due to the trailing edge control surface excitation (δte) in air at 225 psf at Mach 0.5, are shown in Fig. 4. The magnitude plots indicate predominant plunge response at 3.3 Hz excitation frequency. At 4.2 Hz excitation, the motion is a combination of pitch and plunge with pitch motion leading the plunge. The $(zte - zle)$ represents a signal proportional to the pitch acceleration and can be integrated to provide a pitch-rate signal. Feedback of this signal with proper gain can provide maximum pitch damping at the flutter frequency.
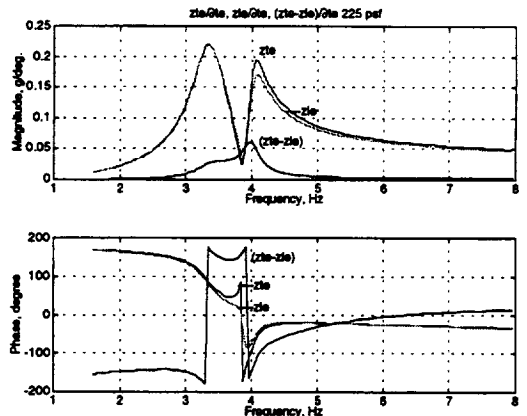

Fig. 4 The Bode diagrams of zte and zle and $(zte - zle)$ due to δte excitation in air at 225 psf, Mach 0.5.

Classical Control Law Design

Based on this Bode plot, a classical flutter suppression scheme using pitch-rate proportional feedback from the zte and zle accelerometers was first devised by studying the Nyquist diagrams. The Nyquist diagram of the difference between trailing edge and leading edge accelerometers $(zte - zle)$ due to the trailing edge control surface excitation (δte) in air at 200 psf, is shown in Fig. 5(a). The arrow indicates increasing frequency of excitation from 2 Hz to 6 Hz, with each * representing frequency increment of 1 radian/second. Since the open-loop plant had a pair of complex unstable poles, and the Nyquist contour did not encircle the −1 point, the unit feedback closed-loop system would be unstable. However, if the $(zte - zle)$ signal was integrated to provide a 90 degree phase lag and then used for feedback with sufficient gain, the Nyquist contour would rotate 90 degrees clockwise and then expand to encircle the −1 point to achieve stability. A washout filter of type $s/(s + a)$ was also required, to remove any static bias that would otherwise be amplified by the integration. The series connection of integrator $1/s$ and washout filter was equivalent to a first order lag filter $a/(s + a)$, where s is the Laplace operator.
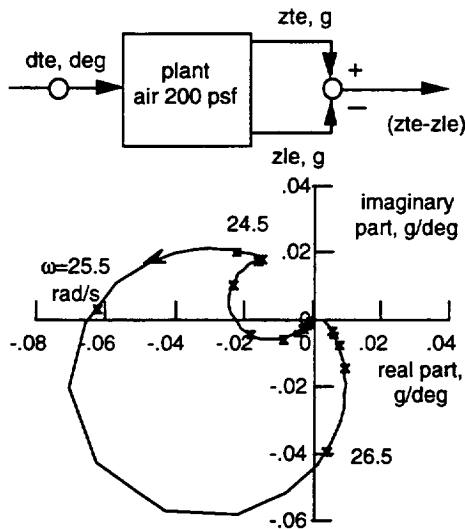

Fig. 5(a) Nyquist diagram of $(zte-zle)$ due to δte excitation in air at 200 psf, Mach 0.5

Gain Selection

Two types of lag filters, namely $5/(s + 5)$ and $10/(s + 10)$ were examined. The latter was selected to achieve a higher phase margin at the plant input above the flutter frequency. Higher phase margin was desirable for two reasons[7]. First, the 25 Hz antialiasing filter and the 1/200 seconds computational delay contribute about 20 degrees of phase lag at the flutter frequency. Secondly, with increasing dynamic pressure, the actuators may have additional unknown phase lag, as the control surface

moves against higher aerodynamic loads. The Nyquist diagram of the difference between trailing edge and leading edge accelerometers $(zte - zle)$ with $10/(s + 10)$ lag filter and a gain $KR = 500$ due to the trailing edge control surface excitation (δte) in air at 200 psf, Mach 0.5, is shown in Fig. 5(b). The unit circle is also shown. Because the Nyquist contour encircled the −1 point, the unit feedback closed loop system would be stable. As desired, the phase margin at the plant input above the flutter frequency was about 60 degrees, but the phase margin below the flutter frequency was only 20 degrees. Preliminary analysis indicated that this basic simple control law 1

$$\delta te = 500\frac{10}{s+10}(zte - zle)$$

can suppress the flutter instability in the dynamic pressure range from 0 to over 225 psf, both in air and in heavy gas medium. However, the closed loop transient responses and stability margins required substantial improvement.
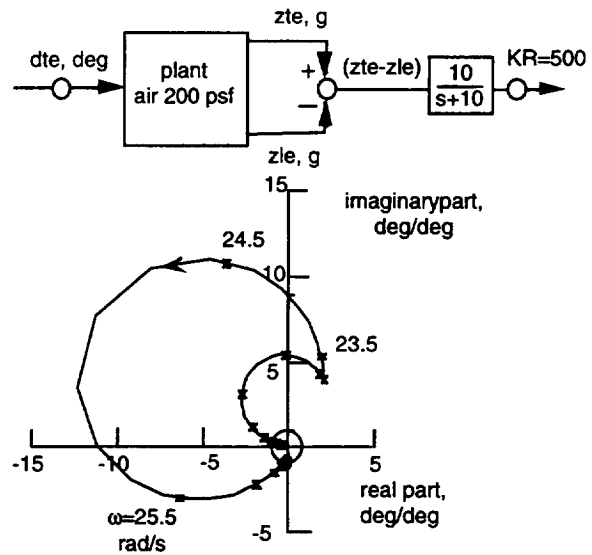

Fig. 5(b) Nyquist diagram of $(zte - zle)$ with $10/(s+10)$ lag filter and a gain $KR = 500$, due to δte excitation in air at 200 psf, Mach 0.5 .

Root Locus

Analysis of the root locus with pitch acceleration $(zte - zle)$ feedback through a $10/(s + 10)$ lag filter with increasing gain $KR = 0, 500, ..., 2500$ is shown in Fig. 6(a). The stabilization was achieved by increasing the pitch model damping and lowering the plunge mode frequency. An additional feedback of the pitch rate proportional signal through a $5/(s + 5)$ lag filter with $KR = 500$ and increasing gain $KP =0,500, ..., 2500$ was used to increase the damping and frequency separation further, as indicated by the root-locus diagram shown in Fig. 6(b).

This design strategy was equivalent to pitch-angle and pitch-rate proportional feedback that increased the pitch mode frequency and plunge mode damping.
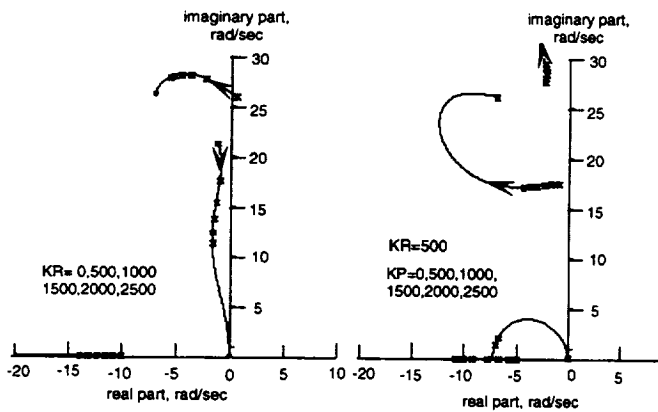

Fig. 6(a) Root-locus with (zte − zle) feedback through a $10/(s + 10)$ lag filter, with increasing gain KR (at left). 6(b) Root-locus with additional pitch-rate feedback through a $5/(s + 5)$ lag filter with $KR = 500$ and increasing gain KP. The arrows indicate increasing gain.

Pitch and Pitch-Rate Feedback Control Law

From the root-locus study, the feedback gains were selected as $KR = 500$ and $KP = 1$. Thus, the second order state space equations of the initial pitch and pitch-rate feedback control law 2 is given by

$$\begin{Bmatrix} \dot{x}_1 \\ \dot{x}_2 \end{Bmatrix} = \begin{bmatrix} -10 & 0 \\ 5 & -5 \end{bmatrix} \begin{Bmatrix} x_1 \\ x_2 \end{Bmatrix} + \begin{bmatrix} 10 & -10 \\ 0 & 0 \end{bmatrix} \begin{Bmatrix} \ddot{z}_{te} \\ \ddot{z}_{le} \end{Bmatrix}$$

$$\delta_{te} = \begin{bmatrix} 500 & 1 \end{bmatrix} \begin{Bmatrix} x_1 \\ x_2 \end{Bmatrix}.$$

The control law inputs are zte and zle in g unit and the output δte is in degrees. The high feedback gain was required because the maximum (zte − zle) signal was only of the order 0.1 g/deg. The response exhibited 2% settling time in 1.5 seconds. However, the high gain resulted in a severe sensitivity with respect to plant perturbation and individual sensor uncertainty, as indicated by the corresponding singular value plots in Fig. 7. Here G, K and Δ denote plant, controller and uncertainty block, respectively[8,9]. This figure indicates that the minimum singular value $\underline{\sigma}$(I+KG) is 0.3 at plant input and $\underline{\sigma}$(I+GK) is only 0.01 at plant output. This means that at 225 psf dynamic pressure, the closed-loop system has very little robustness to multiplicative perturbation[8,9] at the plant output.

These singular value $\underline{\sigma}$ plots can be related to multivariable gain and phase margins using the universal gain and phase margin diagram[8] shown in Fig. 8. For example, minimum singular value $\underline{\sigma}$(I+KG) of 0.3 is

equivalent to ±20 degrees phase and ±3 dB gain margins at the plant inputs. The singular value $1/\underline{\sigma}[K(I+GK)^{-1}]$ is close to 0.005 g/degrees near 2 Hz. This means that the plant has very little tolerance to an additive perturbation Δ to the plant. The complex determinant locus of (I+KG) and its distance from the origin is a measure of its closeness to singularity.
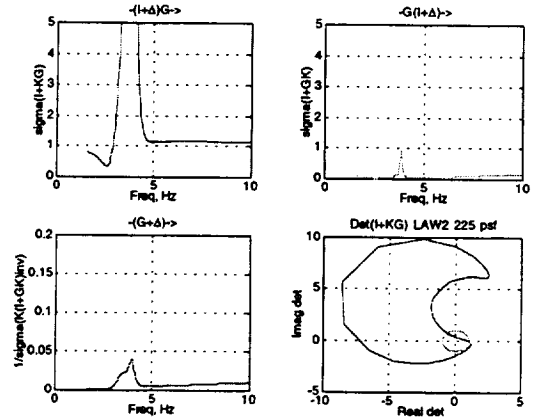

Fig. 7 Singular value plots for analysis of multivariable stability margins to a perturbation Δ, at the plant input or output, with classical control law 2, at 225 psf, in air.
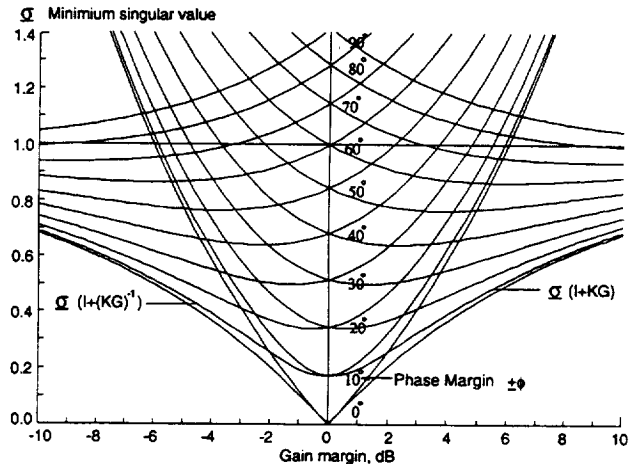

Fig. 8 Universal gain and phase margin analysis diagram.

Final Pitch and Pitch-Rate Feedback Control Law

This lack of robustness associated with this pitch and pitch rate feedback control law was alleviated by choosing a feedback of a proper linear combination of the two sensors with lower gains for KR, instead of using the difference (zte − zle). The linear combination of zte and zle, which is equivalent to feeding back both pitch acceration (zte − zle) and plunge acceleration (zte + zle) in the ratio $0.7(zte − zle) + 0.3(zte + zle)$, appeared to provide a superior control law. The final classical feedback control law, using this combination that is equivalent to (zte - 0.4 zle) feedback, along with reduced

384

gains of $KR = 50$ and $KP = 1$, was analyzed and implemented. The basic control is shown here in state-space form and is denoted by classical control law 3.

$$\begin{Bmatrix} \dot{x}_1 \\ \dot{x}_2 \end{Bmatrix} = \begin{bmatrix} -10 & 0 \\ 5 & -5 \end{bmatrix} \begin{Bmatrix} x_1 \\ x_2 \end{Bmatrix} + \begin{bmatrix} 10 & -4 \\ 0 & 0 \end{bmatrix} \begin{Bmatrix} \ddot{z}_{te} \\ \dot{z}_{te} \end{Bmatrix}$$

$$\{\delta_{te}\} = \begin{bmatrix} 50 & 1 \end{bmatrix} \begin{Bmatrix} x_1 \\ x_2 \end{Bmatrix}$$

Response and Robustness Analysis

The closed-loop transient responses due to 1 degree step deflection of δte, in air at 225 psf, at Mach 0.5, is shown in Fig. 9. The trailing edge control surface shows only 0.25 degrees overshoot with a maximum rate of 12 degrees /sec. The lift and moment forces indicate about 20% load alleviation compared to the open-loop initial transient values shown in Fig. 3. Figure 10 shows the singular-value plots for analyzing the system stability margins[8,9] with law 3 at 225 psf dynamic pressure. Here G, K and Δ denote plant, controller and uncertainty block transfer function, respectively. This figure indicates that the minimum singular value $\underline{\sigma}(I+KG)$ is increased to 0.8 at plant input and at plant output $\underline{\sigma}(I+GK)$ is increased to 0.3 from the corresponding values with law 2 presented in Fig. 7. The minimum singular value $\underline{\sigma}(I+KG)$ of 0.8 is equivalent to ±45 degrees phase and -5 dB to 12 dB gain margins at the plant inputs. These gain and phase margins are determined from Fig. 8 as previously described. The minimum singular value $1/\overline{\sigma}[K(I+GK)^{-1}]$ is also increased from 0.005 g/degree to 0.04 g/degree near flutter frequency, thus increasing the plant's tolerance to additive plant perturbation. The complex determinant loci of (I+KG) ideally should be outside the unit circle to achieve ±6dB gain margins and ±60 degrees phase margins. The computational delay and antialiasing filters added 20 degrees phase lag. Hence, the system nearly attained these margins. The singular value plots indicate that the system is stable with adequate singular value based multivariable stability margins even at this high design dynamic pressure of 225 psf. This pressure is 97 psf above the open-loop flutter dynamic pressure $q_{flutter}$ 128 psf, representing a 75% increase.

Unified Optimal Design

Flutter suppression control law design using an unified (1) linear quadratic Gaussian (LQG) and (2) Minimax method[10,11] is presented next. The Minimax approach is analogous to the time domain H-infinity design[12] and is based on the steady state differential game formulation. The unified formulation of these optimal design techniques provide a basic understanding of the relation between them. The derivation from basic principles using variational principles are provided. The

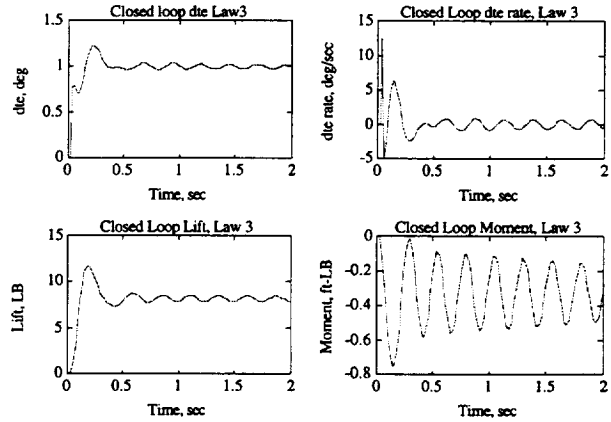solution only requires an eigen-solver. The corresponding Matlab script is presented in the Appendix.

Fig. 9 Closed-loop responses: control surface deflection and rate, lift and pitching moment, due to step input δte with control law 3, at 225 psf, in air, at Mach 0.5 (open loop $q_{flutter}$ =128 psf).
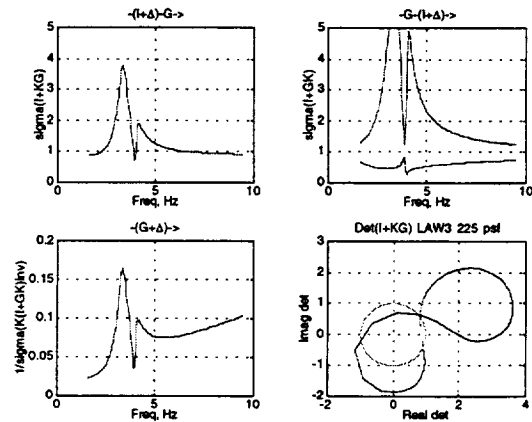
Fig. 10 Singular value plots for analysis of multivariable stability margins to perturbation Δ, with classical control law 3, at 225 psf, in air.

Unified Minimax Formulation

Consider the state space Eqs.(1-3) representing the nth order plant, control input $u(t)$, disturbance $w(t)$, design output y_d and sensor output y_s, where all necessary rank, controllability and observability conditions are assumed to be satisfied.

Plant state-space equations
$$dx(t)/dt = F\,x(t) + G\,u(t) + G_w\,w(t)$$
and $x(0) = x_0$ (1)
Design output
$$y_d(t) = H_d\,x(t) + E_{du}\,u(t)$$ (2)
Sensor output
$$y_s(t) = H_s\,x(t) + E_{sw}\,w(t)$$ (3)

385

State-Feedback Minimax Regulator Problem

The Minimax problem is to determine the plant input $u(t)$ which would minimize the quadratic performance index J, and find the worst plant disturbance $w(t)$ and initial condition x_0, which would maximize J defined in Eq. (4),

$$J = \frac{1}{2}\int_0^\infty (x^T Q_x x + x^T Q_{xu} u + u^T Q_u u)dt \tag{4}$$

subject to the constraint Eq.(1) with $x_0^T x_0 = 1$ and specified W defined by,

$$W = \frac{1}{2}\int_0^\infty (w^T R_w w)dt \tag{5}$$

Usually, the constant weighting matrices Q_x, Q_u are unity, and $Q_{xu} = [0]$ in a H-infinity exposition. These are included herein to derive a unified general time-domain formulation. The cross weighting matrix Q_{xu} originates if one uses y_d from Eq. (2) in the performance index J to replace x. Then, $Q_x = H_d^T Q_{yd} H_d$, $Q_{xu} = H_d^T Q_{yd} E_{du}$, and Q_u is replaced by $[Q_u + E_{du}^T Q_{yd} E_{du}]$. The significance of the cross weighting matrix Q_{xu} and how it can be selected for pole-placement of the state regulator will be shown later in the state-feedback regulator subsection.

The minimax solution is given by the stationary condition of the augmented performance index J

$$J = \frac{1}{2}\int_0^\infty (x^T Q_x x + 2x^T Q_{xu} u + u^T Q_u u - \gamma^2 w^T R_w w)dt$$
$$+ \lambda^T \int_0^\infty (Fx + Gu + G_w w - \frac{dx}{dt})dt + \gamma^2 W \tag{6}$$

where, γ is a scalar parameter. Using the calculus of variation with respect to $x(t)$, $u(t)$, $w(t)$ and the vector Lagrange multiplier $\lambda(t)$, the conditions for $\partial J=0$ are given by Eq.(1) and Eqs. (7) to (9).

$$d\lambda/dt = -Q_x x - F^T\lambda - Q_{xu}u \tag{7}$$

$$Q_u u = -G^T\lambda - Q_{xu}^T x \tag{8}$$

$$\gamma^2 R_w w = G_w^T\lambda \tag{9}$$

Solving for $u(t)$ and $w(t)$ from Eqs. (8-9) and substituting them in Eqs. (1) and (7), the necessary stationary conditions for J are obtained as,

$$u = -Q_u^{-1}(G^T\lambda + Q_{xu}^T x) \tag{10}$$

$$w = \gamma^{-2} R_w^{-1} G_w^T \lambda \tag{11}$$

$$\begin{Bmatrix} \dfrac{dx}{dt} \\ \dfrac{d\lambda}{dt} \end{Bmatrix} = \begin{bmatrix} (F - GQ_u^{-1}Q_{xu}^T) & (-GQ_u^{-1}G^T + \gamma^{-2}G_w R_w^{-1}G_w^T) \\ -(Q_x + Q_{xu}Q_u^{-1}Q_{xu}^T) & -(F - GQ_u^{-1}Q_{xu}^T)^T \end{bmatrix} \begin{Bmatrix} x(t) \\ \lambda(t) \end{Bmatrix}$$

with $x(0) = x_0$ and $\lambda(\infty) = 0$ \hfill (12)

State-Feedback Regulator

Substituting $\lambda(t) = S(t)x(t)$, in Eqs.(10-12), leads to Eqs.(13-15). The general Riccati Equation (15) is then solved for the unknown n by n matrix S.

$$u(t) = -Q_u^{-1}(G^T S + Q_{xu}^T)x(t) \tag{13}$$

$$w(t) = \gamma^{-2} R_w^{-1} G_w^T S x(t) \tag{14}$$

$$dS/dt + SF + F^T S + Q_x - (SG + Q_{xu})Q_u^{-1}(SG + Q_{xu})^T$$
$$+ S(\gamma^{-2} G_w R_w^{-1} G_w^T)S = 0 \tag{15}$$

The positive definite symmetric solution for S is obtained from the $(2n \times n)$ eigenvectors of the n stable eigenvalues of the Hamiltonian matrix inside the square bracket [ ] in Eq.(12). For the steady state problem (i.e. $dS/dt = 0$), only the steady part of the Riccati Equation (15) is solved in order to obtain the symmetric positive-definite matrix S. If the eigenvectors are partitioned into two $n \times n$ matrices X and Λ which represent the stable subspace eigenvectors of x and λ, then $S = X^{-1}\Lambda$. The constant optimal feedback gains, C_O and C_W, and the closed-loop system matrix are given by,

$$C_O = -Q_u^{-1}(G^T S + Q_{xu}^T) \tag{16}$$

$$C_W = \gamma^{-2} R_w^{-1} G_w^T S \tag{17}$$

$$dx/dt = [F + G_w C_W + G C_O]x. \tag{18}$$

Using Eqs.(1),(15) and (18), it can be shown[11] that optimal J and W defined in Eqs.(4) and (5) are given by,

$$J = 0.5 \, Trace \, [S] \tag{19}$$

$$W = 0.5 \, Trace \, [C_W^T R_w C_W X]. \tag{20}$$

where X is the solution of the Lyapunov Equation (21)

$$[F + G_w C_W + G C_O] X + X[F + G_w C_W + G C_O]^T + x(0)x(0)^T = [0] \tag{21}$$

The worst $x(0)$ that maximizes J is given by the eigenvector of the maximum eigenvalue of S. The

standard linear quadratic regulator (LQR) solution is obtained when $\gamma = \infty$, (i.e. $C_w = 0$). As γ^2 is decreased, the worst response due to the disturbance w(t), measured by the maximum singular value of $[x^T Q_x^{1/2} \quad u^T Q_u^{1/2}]$, is reduced. The minimum value of γ^2 for which a stable solution of Eq. (15) exists provides the minimax state-feedback regulator that minimizes the maximum singular value of $[x^T Q_x^{1/2} \quad u^T Q_u^{1/2}]$.

The State-Estimator Equation

The derivation of coupled state-estimator equations using linear quadratic minimax approach is still a subject of research. Here the equivalent state-space solutions[12] of the H-infinity problem are presented. The state estimator gain $B_o D_o$ is obtained by finding the symmetric positive definite solution for P from the state estimator Riccati Eq. (24) which is dual to the state regulator Riccati Eq. (15).

$$B_o = -(PH_s^T + R_{wv})R_v^{-1} \qquad (22)$$

$$D_o = (I - \gamma^{-2}PS)^{-1}, \quad \rho(PS) < \gamma^2 \qquad (23)$$

$$dP/dt = PF^T + FP + G_w R_w G_w^T - (PH_s^T + R_{wv}) R_v^{-1}$$
$$(PH_s^T + R_{wv})^T + P(\gamma^{-2} Q_x)P \qquad (24)$$

where $R_v = E_{sw}R_w E_{sw}^T$ and must be positive definite and $R_{wv} = G_w R_w E_{sw}^T$. In Eq. (23) the spectrum $\rho[PS]$ must me less than γ^2 for D_o to exist. The positive definite symmetric steady-state solution for P in Eq. (24) is obtained from the $(2n \times n)$ eigenvectors of the n stable eigenvalues of the estimator Hamiltonian matrix,

$$\begin{bmatrix} (F - R_{wv}R_v^{-1}H_2)^T & (-H_2^T R_v^{-1}H_2 + \gamma^{-2}H_1^T Q_{y1}^{-1}H_1) \\ -G_w R_w G_w^T - R_{wv}R_v^{-1}R_{wv}^T & -(F - R_{wv}R_v^{-1}H_2) \end{bmatrix} \qquad (25)$$

which is dual to the state regulator Hamiltonian matrix inside [ ] in Eq.(12). If the eigenvectors are partitioned into two (n x n) matrices $\underline{X}$ and $\underline{A}$, then $P = \underline{X}^{-1}\underline{A}$. The state estimate vector z is given by the Eq. (26).

$$dz/dt = Fz + G_w w + Gu + D_o B_o(H_2 z - y_2) \qquad (26)$$

The complete duality relations between the state regulator problem and the state estimator problem are presented in Table 1.

state regulator	state estimator
F	F^T
G	H_s^T
G_w	H_d^T
Q_x	$G_w R_w G_w^T$
Q_u	R_v
S	P
Q_{xu}	R_{wv}
$(t_f - t)$	$(t - t_0)$

Table 1. Duality relations between linear quadratic state-regulator and state-estimator equations.

The Controller Equation

Substituting Eqs. (13), (14), (22) and (23) in Eq. (26), the state-estimation feedback controller equations

$$dz/dt = [F + G_w K_w + GC_o + D_o B_o H_s] z - D_o B_o y_s \qquad (27)$$

$$u = C_o z \qquad (28)$$

are obtained. The standard LQG solution is obtained when $\gamma = \infty$. The minimum value of γ^2 for which a stable solution exists for P in Eqs. (22-24), provides the minimax control law that minimizes the maximum singular value of the matrix $[y_s^T Q_{ys}^{1/2} \quad u^T Q_u^{1/2}]$, for the closed loop system.

Unified Design Procedure

In this design, the output y_d was chosen to be the linear combination of the trailing edge and leading edge accelerometer output $(zte - 0.4\ zle)$, same as that used in the final classical design. One advantage of this choice was that the plant had no transmission zeros in the open right half plane. Usually in a frequency domain H-infinity design, the plant equations are augmented with weighting transfer functions. In this time domain formulation, the weights were chosen as constants. These weighting constants are chosen as inverse of the desired magnitude of the weighted quantities. The initial controller was designed with a large value of γ^2, using the plant Eqs. (1-3), at 225 psf, in air, at Mach 0.5, assuming $G_w = G$. The block diagram for this unified design procedure is shown in Figure 11. The detailed design steps are described next.

State-feedback Regulator Design

Initially, the maximum output of the accelerometer sensors were of the order $0.1g$, (see figure 3), and control surface maximum root-mean-square deflection was desired to be of the order 1 degrees. Thus, the initial values of the weighting matrices were chosen as follows: $Q_x = [H_s^T Q_{ys}H_s]$, $Q_{ys} = [100]$, and $Q_u = [1]$. It was interesting to note that, instead of setting the cross weighting matrix $Q_{xu} = [0]$ as usual practice, the cross weighting matrix Q_{xu} can be selected to place all state

regulator poles beyond a certain distance α to the left of imaginary axis. This selection is accomplished by using

$$Q_{xu} = -\alpha G_u (G_u^T G_u)^{-1} Q_u \qquad (29)$$

so that in Eq. (12), the eigenvalues of the diagonal matrix block F are off-set by

$$G Q_u^{-1} Q_{xu}^T = -\alpha I. \qquad (30)$$

The control-weighting matrix Q_u was subsequently reduced to 0.01 after a few design cycles to improve the regulator performance. This process of reducing Q_u is equivalent to the state estimator loop-transfer recovery technique at the plant output.
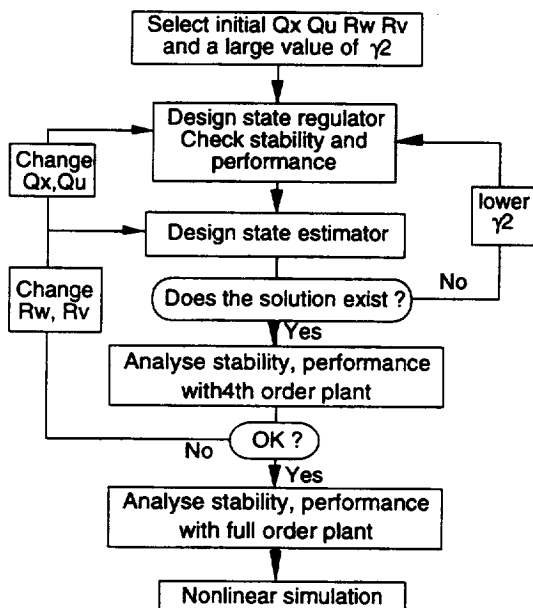

Fig.11. Unified minimax control law design and evaluation procedure block diagram.

State-estimator Design

The state estimator was designed as a dual to the state-regulator with $R_w = 1$, each diagonal elements of $R_v = 0.01$, and $R_{wv} = [0]$. After a few design cycles the performance of the combined full-order controller was examined, and then R_w was increased to 36. Since we also choose $G_w = G$, this was equivalent to asymptotic state-regulator loop-transfer recovery at the plant input.

4th Order Optimal Control law

Subsequent solutions to the state-regulator and state-estimator were obtained with the same choice of weighting matrices but for decreasing value of γ^2, for which positive definite solutions for S and P could be obtained. Note that feasible solutions can be obtained for

lower values of γ^2 up to $\gamma^2 > \rho(PS)$, below which the disturbance authority exceeded the control authority. The 4th-order optimal control law was designed with $\gamma^2 = 50$ in order to obtain a low bandwidth controller. Fig. 12 shows the key singular value plots for analysis of multivariable stability margins to multiplicative and additive perturbation Δ at the plant input and output, with this minimax optimal control law, denoted as control law 4. The minimum singular value $\underline{\sigma}(I+KG)$ is increased to 0.9 at plant input and at plant output $\underline{\sigma}(I+GK)$ is increased to 0.5 from the corresponding values of 0.8 and 0.3 for control law 3, shown in Fig. 10.
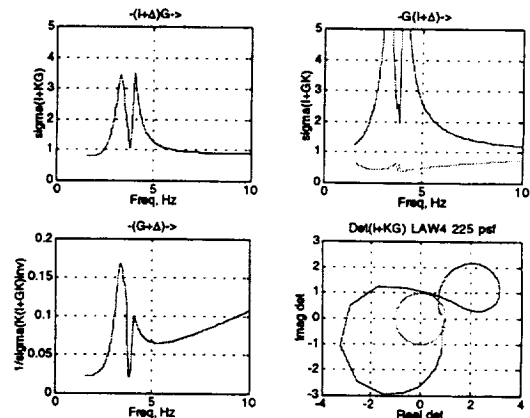

Fig. 12 Singular value plots for analysis of multivariable stability margins with minimax optimal control law 4, at 225 psf, in air.
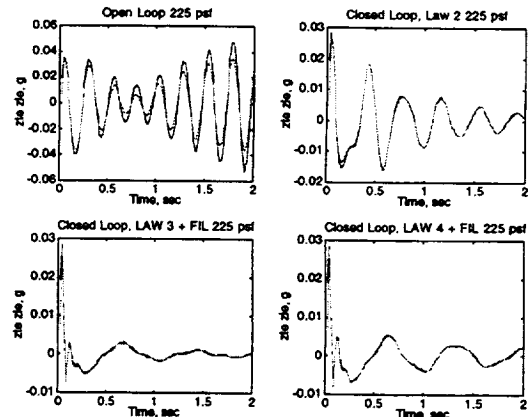
Fig. 13 Open-loop and closed-loop responses due to step input δte, with classical control laws 2, and 3, and minimax optimal control law 4, at 225 psf, in air.

Fig.13 shows the open-loop and closed-loop responses due to unit step input δte of trailing edge control surface, at 225 psf, in air, at Mach 0.5, with initial control law 2, classical control law 3, and minimax optimal control law 4. The transient responses indicate

388

that the classical control law 3 provided better damping with lower control surface activity although the minimax control law 4 provided better robustness properties. This is the traditional trade-off between performance and robustness. The classical control law 3 was implemented and tested in wind tunnel. These test results along with those using two optimal control laws designed by Waszak[13] are presented next.

Flutter Suppression Test Results

The performance and robustness of the final design was tested using the original full plant state-space equations and filters required for digital implementation. The 25 Hz antialiasing filters $157/(s+157)$ were added to the plant output. The washout filter $5s/(s+5)$ and computational delay were added to the controller output equations. The $1/200$ second computational delay was modeled by a $(400-s)/(400+s)$ filter. Before the wind-tunnel test entry, the digital implementation was also numerically simulated. The numerical simulation block diagram of the control system using the final classical control law 3 is shown in Figure 14. This nonlinear simulation also included the effects of a dead-band present in the electro-hydraulic actuator. Application of the upper and lower spoiler for transonic flutter suppression with the same digital control law was also investigated using this simulation.

The active flutter suppression control-law using classical design was successfully tested in air and in heavy gas medium at transonic speeds up to Mach 0.95. The tests in air indicated an increase in the flutter instability boundary from the open-loop dynamic pressure of 158 psf (Mach 0.38) to the tunnel limit of 200 psf. A summary of flutter suppression test results in heavy gas is shown in Fig. 15. The solid line indicates the experimental flutter boundary, with the transonic dip at Mach 0.8. The tests at Mach 0.8 indicated an increase in the flutter stability boundary from the open-loop dynamic pressure of 142 psf to the tunnel upper limit of 200 psf. A non-design plunge instability condition was also successfully suppressed. Classical control law 3 exhibited superior performance and was demonstrated to be stable with gain variation from 0.25 to 7, and phase variation from -90 to 60 degrees. A non-design plunge instability condition was also successfully suppressed. Comparison of open-loop and closed-loop root mean square (RMS) responses of trailing edge accelerometer and control surfaces using the present classical control law 3 and two other control laws designed by Waszak[13] are shown in Figs. 16 and 17, respectively. These two control laws used upper and lower spoilers as control surface, for flutter suppression. Fig. 16 indicates that when the system is open loop stable, closing the loop actually reduces the response by 30%. Fig. 17 indicates that that the classical control law 3 generally requires less control activity. All three control

laws are comparable in performance, with control law 3 exhibiting higher stability margins.
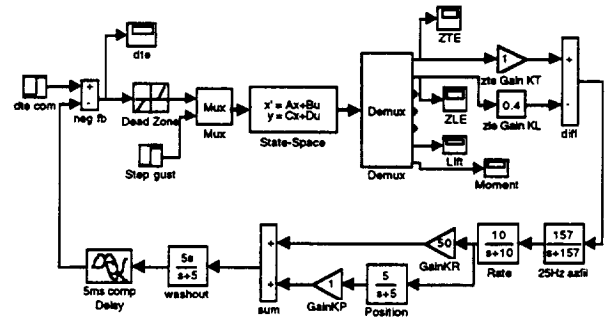

Fig.14 Numerical simulation block diagram of the control system implementation using the final classical control law 3 for flutter suppression.
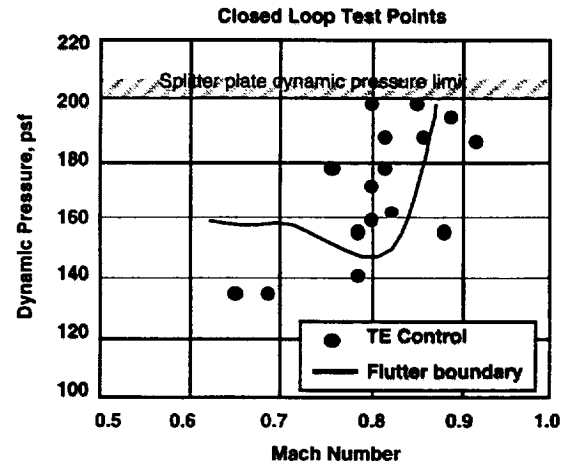

Fig. 15 Open-loop flutter boundary and closed-loop flutter suppression results from wind-tunnel tests in heavy gas.
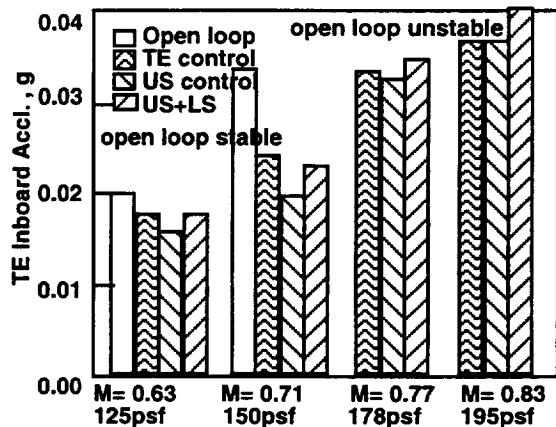

Fig. 16 Open-loop and closed-loop RMS responses with classical control law 3 and two control laws employing spoilers from wind-tunnel tests in heavy gas medium.

389

Conclusions

Simple classical control laws, when properly designed based on physical principle, can successfully suppress transonic flutter and provide significant stability robustness in presence of shock and flow separation. Comparable robust optimal control laws can also be designed using a new generalized unified minimax formulation. Verification and improvement of the multivariable system stability robustness to unstructured perturbations at the plant, input and output were important steps in such a design process. Wind-tunnel tests in air and heavy gas indicated an increase in the transonic flutter dynamic pressure to the tunnel limit upper limit of 200 psf. The control law robustness and performance predictions were verified in highly nonlinear flow conditions, gain and phase perturbations, and spoiler deployment.
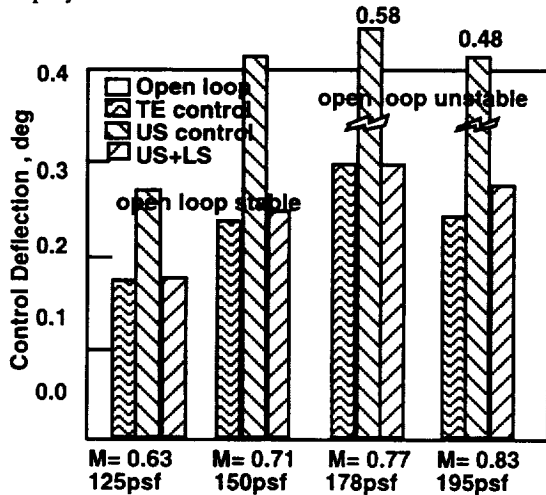

Fig. 17 RMS responses of the control surfaces with the classical control law 3 and two control laws from wind-tunnel tests in heavy gas medium.

References

[1]Bennett, R. M.; Eckstrom, C.V.; Rivera, J. A. Jr., Dansberry B. E.; Farmer M. G.; and Durham, M.H.: The Benchmark Aeroelastic Models Program - Description and Highlights of Initial Results. NASA TM 104180, 1991.

[2]Rivera, J. A. Jr.; Dansberry B. E.; Farmer M. G.; Eckstrom, C.V.; Seidel, D. A.; and Bennett, R. M.: Experimental Flutter Boundaries with Unsteady Pressure Distribution for the NACA 0012 Benchmark Model. AIAA Paper No. 91-1010, 1991 (NASA TM-104072, 1991)

[3]Rivera, J. A. Jr.; Dansberry B. E.; Bennett, R. M.; Durham, M.H. and Silva, W. A.: NACA 0012 Benchmark Model Experimental Flutter Results with Unsteady Pressure Distribution. AIAA Paper No. 92-2396, April 1992.

[4]Durham, M.H.; Keller, D.F.; Bennett, R. M.; and Wieseman, C. D.: A Status Report on a Model for Benchmark Active Control Testing. AIAA Paper No. 91-1011, 1991.

[5]Hoadley, S. T.; and Adams, W.M. Jr.: ISAC - Interaction Structures, Aerodynamics, and Controls. Version 5.1 Sample Cases with Guides for UNIX Operating Systems, NASA TM-100667, January, 1992.

[6]Mukhopadhyay, V.: Flutter Suppression Control Law Design and Testing for the Active Flexible Wing, Journal of Aircraft (Special Adaptive Flexible Wing Issue) Vol. 32, No. 1, Jan-Feb. 1995, pp. 45-51.

[7]Perry, B. III; Cole, S. R.; and Miller, G. D.: A Summary of an Active Flexible Wing Program," Journal of Aircraft , Vol. 32, No. (1995), pp.10-15.

[8]Mukhopadhyay, V.: Stability Robustness Improvement Using Constrained Optimization Techniques. Journal of Guidance, Control, and Dynamics, Vol. 10, No. 2, March-April 1987, pp. 172-177.

[9]Pototzky, A. S.; Wieseman, C. D.; Hoadley, S. T.; and Mukhopadhyay, V.: On-line Performance Evaluation of Multiloop Digital Control Systems, Journal of Guidance, Control, and Dynamics, Vol. 15, (1992), pp. 878-884.

[10]Bryson, A. E. Jr.; and Carrier, A.: A comparison of Control Synthesis Using Differential Games (H-Infinity) and LQR. AIAA Paper 89-3598 CP, August 1989.

[11]Ghaoui, E., L.; Carrier, A.; and Bryson, A. E. Jr.: Linear Quadratic Minimax Controllers. Journal of Guidance, Control, and Dynamics, Vol. 15, No. 4, July-August 1992, pp.953-951.

[12]Doyle, J. C.; Glover K.; Khargonekar, P. P.; and Frances, B. A.: State-Space Solutions to Standard H2 and H-Infinity Control Problems. IEEE Transactions on Automatic Control, Vol. 34, No. 8, August 1989, pp.831-847.

[13]Waszak, M. R.: Robust Multivariable Flutter Suppression for the Benchmark Active Control Technology (BACT) Wind-Tunnel Model, Proc. 11th Symposium on Structural Dynamics and Control, VPISU, Blacksburg,VA,1997.

Appendix

Reduced 4th order state space equations in air at 225 psf. and Matlab script for unified minimax formulation and solution

$$F = \begin{bmatrix} -1.6073 & 21.0010 & 0. & 0. \\ -21.0010 & -1.6073 & 0. & 0. \\ 0. & 0. & 0.7515 & 25.1670 \\ 0. & 0. & -25.1670 & 0.7515 \end{bmatrix}$$

$$[G \ G_w] = \begin{bmatrix} -3.8259 & 0.0597 \\ 12.7130 & 0.2720 \\ -2.2202 & -0.1107 \\ 4.1351 & -0.1745 \end{bmatrix}$$

$H_d = $ [-0.0517   -0.0132   -0.0668   0.0063
         -0.0542   -0.0090   -0.0482   -0.0016
          0.   0.   0.   0.
          0.   0.   0.   0.
          0.   0.   0.   0.
         10.3780   0.6369   7.9924   0.0671
          0.3897   -0.9373   -2.7625   0.9909]

$[E_{du}\ E_{dw}] = $ [0.0440   0.0002
                        0.0421   0.0004
                        1.0000   0.
                       50.0000   0.
                        0.   0.0968
                        0.5758   -0.0004
                        0.0358   -0.0003]

```
% Matlab script for unified formulation and solution
% xdot = F x +  Gw w  + G u
%  yd = Hd x + Edw w + Edu u   Design output
%  ys = H x  + Esw w + Esu u   Sensor output
% 7 design output [zte zle dte ddte gust lift moment]
% -------------------------------------------------
Q11 = h'*qh*h+hd'*qhd*hd;
Q22 = [q2]+[Edu'*qhd*Edu];
% pole placement using cross weight Q12
   alpha = 3.0;
Q12=-alpha*g*((g'*g)\Q22)+[hd'*qhd*Edu];
WW  =[Q11   Q12 ; Q12'   Q22 ];
% Generalized LQR Weights
Ru = [gw*rw*gw'+nu*g*g'];
Rv = [rv]+[Esw*rw*Esw'];
Rwv = [gw*rw*Esw'];
% generalized EST Weights
VW = [Ru  Rwv ; Rwv'  Rv ];
% Generalized DESIGN with Edw=0
[af,bf,cf,df]=lqg(f,g,h,Edu,WW,VW);
%----------------------------------------
% STATE REGULATOR
% Check if Q11 is positive semi-definite and symmetric
if any(eig(Q11) < -10*eps) | (norm(Q11'-Q11,1)/norm
(Q11,1) > eps)
error('Q11 must be symmetric positive semi-def), end
% Check if Q22 is positive definite and symmetric
if any(eig(Q22) <= 0) | (norm(Q22'-Q22,1)/norm(Q22,1)
> eps)
error('Q22 must be sym. positive definite'), end
%-------------------------------------------------
% Construct Hamiltonian
Hm=[(f-g*[Q22\Q12']) -g*[Q22\g']+gw*[rw\gw']/mu
-Q11-Q12*[Q22\Q12']   -(f-g*[Q22\Q12'])'];
[v,d]=eig(Hm);
%-------------------------------------------
% Sort eigen vector of neg eigenvalues
d = diag(d);
[d,index] = sort(real(d));
if (~( (d(n)<0) & (d(n+1)>0) ))
error('Can''t order eigenvalues'), end
% select vectors with negative eigenvalues
chi = v(1:n,index(1:n));
lambda = v((n+1):(2*n),index(1:n));
S = real(lambda/chi);
%------------------------------------------
% Positive feedback gain ku
ku=-Q22\(g'*S+Q12');
kw=[rw\gw']*S/mu;
%------------------------------------------
% closed loop plant f = fcl
fcl=f+g*ku+gw*kw;
X=lyap(fcl,eye(n)) % assume xo*xo'=I
Xg=lyap(fcl,gw*gw'*36)
W=0.5*trace(kw'*rw*kw*Xg)
Jo=0.5*trace(S)
Uu=trace(ku'*ku*Xg)
Ycov=Hd*Xg*Xg'*Hd'
%------------------------------------------
% H-inf ESTIMATOR DESIGN
% define Hamiltonian Jam
Ru = [gw*rw*gw'+nu*g*g'];
J = [ (f-[Rwv/Rv]*h)'   [-h'/Rv]*h+[hd'/qhd]*hd/mu
      -Ru-[Rwv/Rv]*Rwv'    -(f-[Rwv/Rv]*h) ];
[v,d]=eig(J);
%------------------------------------------
% sort eigenvector of stable eigenvalues
d = diag(d); [d,index] = sort(real(d));
% sort on real part of eigenvalues
if (~( (d(n)<0) & (d(n+1)>0) ))
error('Can''t order eigenvalues'), end
%------------------------------------------
% select vectors with negative eigenvalues
chi = v(1:n,index(1:n));
lambda  =  v((n+1):(2*n),index(1:n));
P  = real(lambda/chi);
ky = -(P*h'+Rwv)/Rv;
% check positive definiteness of kd
% Is this matrix (I - P*S/mu) nonsingular ?
mumin=max(abs(eig(P*S)))
if (mu > mumin),
kd = inv(eye(n)-(P*S)/mu); , else
error('spectrum(P*S) > mu , increase mu'), end
%------------------------------------------
eve=eig(f+kd*ky*h);
% controller structure
   Ao=f+g*ku+gw*kw+kd*ky*h;
   evc=eig(Ao);
% H-infinity controller
% Kop = [Ao -kd*ky -ku  zeros(nc,ns)];
[fc, gc ,hc, ec] = feedback(f, g, h, e, Ao, -kd*ky ,-ku,
zeros(nc, ns));
%-------------------------------------------
```